ACS APPLIED ENERGY MATERIALS

www.acsaem.org

Article

Analysis of Se Co-evaporation and Post-selenization for Sb_2Se_3-Based Solar Cells

Vikash Kumar, Elisa Artegiani, Prabeesh Punathil, Matteo Bertoncello, Matteo Meneghini, Fabio Piccinelli, and Alessandro Romeo*

Cite This: *ACS Appl. Energy Mater.* 2021, 4, 12479−12486

Read Online

ACCESS | Metrics & More | Article Recommendations

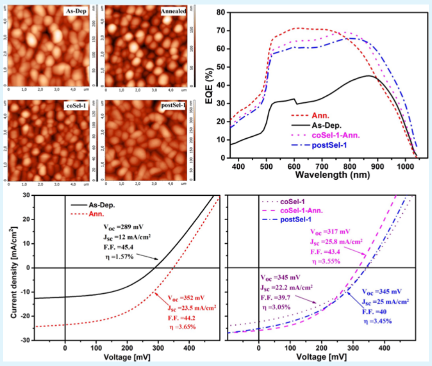

ABSTRACT: Sb_2Se_3 is a promising alternative absorber material for thin-film solar cells. However, by a thermal evaporation technique, it appears to partially decompose, leading to Se deficiency. In this work, we propose two alternative routes for the supply of selenium in the deposition of Sb_2Se_3 thin films. The first method is the co-evaporation of Se and Sb_2Se_3, while the second is the post-deposition selenization. Superstrate glass/FTO/TO/CdS/Sb_2Se_3/Au-configured thin-film cells are grown using thermal evaporation. X-ray diffraction patterns confirm the presence of CdS peaks along with the preferred ($hk1$) oriented grains, which are suppressed upon selenization. Modified surface morphology for the selenized samples is observed by atomic force microscopy. Enhanced current density is observed by $J-V$ characterization and also confirmed by a remarkable external quantum efficiency (EQE) gain at long wavelengths. However, CdS deterioration reduces the EQE response in the short wavelength region, acting as a limiting factor for the efficiency improvement. The champion cell shows a power conversion efficiency of 3.6% with an open circuit voltage of 352 mV and a fill factor of 44.2%, which results in, to our knowledge, the highest value for thermally evaporated Sb_2Se_3 in superstrate configuration.

KEYWORDS: *Sb_2Se_3, Se, evaporation, thin films, solar cell*

INTRODUCTION

Cadmium telluride (CdTe) and copper indium gallium diselenide (CIGS) are optimal thin films with high absorption coefficients and excellent electronic properties for high power conversion efficiency (PCE), with the value for CIGS exceeding 23%.[1] Despite such remarkable features, these materials are limited by the scarcity of In and Te that could limit the fabrication in a large scale; hence, other materials are being evaluated.

Some important chalcogenide compounds made of earth-abundant elements with attractive photovoltaic (PV) properties are Cu_2SnS_3,[2] $CuSbS_2$,[3] $Cu_2ZnSnSe_4$,[4] $CuSbSe_2$,[5] $Sb_2(S,Se)_3$,[6] and Sb_2Se_3.[7] In the past decade, antimony selenide has emerged as a promising alternative absorber material. Sb_2Se_3 is a simple binary compound with a very high absorption coefficient of 10^5 cm^{-1} (needing a very thin layer below 1 μm), and selenium and antimony are rather abundant on the earth crust; however, antimony is categorized as a critical raw material since it is very abundant but mostly in the Chinese territory. Moreover, this compound has a suitable band gap that can be tuned from 1.1 to 1.3 eV, allowing a theoretical PCE of 30% by a Shockley−Queisser efficiency limit with a long carrier lifetime (~60 ns).[7] Sb_2Se_3 has an orthorhombic crystal structure ($Pbmn$ space group) with lattice constants of about a = 11.63 Å, b = 11.78 Å, and c = 3.985 Å.[8,9]

The one-dimensional (1D) crystal structure of Sb_2Se_3 has $[Sb_4Se_6]_n$ units, where the ribbons are bound together by weak van der Waals forces. Grain boundaries, which are parallel to the ribbons, reduce charge-carrier recombination and are beneficial for the PV device performance.[10,11] The highest PCE obtained so far is 9.2% by close space sublimation;[12] on the other hand, Sb_2Se_3 grown by thermal evaporation on superstrate and substrate configuration has provided efficiencies of 1.9 and 2.1%, respectively.[13,14]

Studies performed by Liu et al. indicate that Sb_2Se_3 films partly decompose during thermal evaporation, leading to Se deficiency. This generates, in the Sb_2Se_3 bulk, selenium vacancies (V_{Se}), giving place to deep recombination centers that affect the performance of the device.[14]

In this paper, we explore two methods to mitigate the Se loss: (a) by simultaneously evaporating Sb_2Se_3 and Se during the absorber growth (co-selenization) or (b) by post-deposition selenization, which results in a two-step process

Received: August 2, 2021
Accepted: October 10, 2021
Published: October 19, 2021

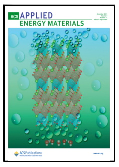

where in the first step, Sb_2Se_3 is deposited on the buffer layer and then, in the second step, Se is fluxed at 350 °C. The influence of selenization on the Sb_2Se_3 thin films was investigated by atomic force microscopy (AFM), X-ray diffraction (XRD), Raman spectroscopy, external quantum efficiency (EQE) measurement, and current−voltage (*J*−*V*) characterization.

EXPERIMENTAL DETAILS

Sb_2Se_3 solar cells are prepared in superstrate configuration (glass/FTO/TO/CdS/Sb_2Se_3/Au). The front contact (TCO, transparent conductive oxide) consists of a fluorine-doped tin oxide (FTO) layer followed by a high resistivity transparent (HRT) undoped tin oxide (SnO_2 $\rightarrow$ TO) layer industrially deposited on soda lime glass (NSG TEC 12D). CdS is deposited on the FTO/TO stack by thermal evaporation at a pressure of 10^{-4} Pa with a substrate temperature of 150 °C and a thickness of 150 nm. The presence of the HRT layer allows reducing the CdS thickness, avoiding shunts between the CdS layer and the FTO layer and increasing the open circuit voltage. After deposition, the layer is annealed in the same deposition chamber in vacuum at 450 °C to improve its crystalline structure and its stability for subsequent depositions.

The absorber thickness has been optimized and fixed to 450 nm, and the layer is deposited at a substrate temperature of 300 °C with a base pressure of 3×10^{-4} Pa.

During the co-selenization process, Se powder is evaporated simultaneously with Sb_2Se_3 from distinct graphite crucibles at different rates. Selenium rates (R_{Se}) have been fixed relative to the evaporation rate of Sb_2Se_3 (R_{Sb2Se3}), in particular we have considered $R = 2$, $R = 1$, and $R = 0.5$ with $R = R_{Se}/R_{Sb2Se3}$. The post-deposition heat treatment of as-deposited and co-selenized samples is done at 350 °C.

Post-deposition selenization is instead performed directly at a substrate temperature of 350 °C; the rate of the additional Se evaporation step is also calculated based on the previous Sb_2Se_3 deposition rate: $R = R_{Se}/R_{Sb2Se3}$. The details of the samples along with their ID are presented in Table 1,ba. The Sb_2Se_3 lumps and Se pellets are heated in graphite crucibles at temperature ranges of 600−700 and 280−350 °C, respectively.

Table 1. (a) As-deposited, Annealed, and Co-selenized Samples and (b) Post-deposition Selenized Samples

(a) sample I.D.	co-selenization	post-deposition heat treatment (°C)
As-Dep		
coSel-1	$R = 1$	
Ann		350
coSel-0.5-Ann	$R = 0.5$	350
coSel-1-Ann	$R = 1$	350
coSel-2-Ann	$R = 2$	350

(b) Ssample I.D.	post-selenization heat treatment (350 °C)
postSel-0.5	$R = 0.5$
postSel-1	$R = 1$
postSel-2	$R = 2$

The back contact consists of a 30 nm-thick Au film deposited by thermal evaporation at a base pressure of 1×10^{-3} Pa followed by post-deposition annealing at 150 °C in air.

The crystalline structure of the samples was studied using XRD, carried out with a Thermo ARL XTRA powder diffractometer in Bragg−Brentano geometry, equipped with a Cu-anode X-ray source ($K\alpha, \lambda = 1.5418$ Å) and a Peltier Si (Li) cooled solid-state detector. AFM was conducted using an NT-MDT Solver Pro in semicontact mode with an NSG-01 silicon tip. Raman spectra were obtained with a Horiba Jobin-Yvon LabRam HR800 microprobe setup (in backscattering geometry) by using an excitation radiation at 532 nm (He−Ne laser). *J*−*V* characteristics were measured with a Keithley Source Meter 2420 using a halogen lamp calibrated with a silicon solar cell under an irradiation of 100 mW/cm^2. The external quantum efficiency (EQE) spectra were acquired using a commercial LOANA solar cell analysis system, calibrated with a silicon reference sample with known EQE using an incident spotlight of a 1 mm × 2 mm area.

RESULTS AND DISCUSSION

The XRD patterns for the differently grown Sb_2Se_3 films are shown from Figures 1 to 3. They consist of well-resolved peaks, which have been indexed to the *Pbmn* space group in orthorhombic symmetry. All the diffraction peaks of the thin films were well matched with the JCPDS card no. PDF 15-0861. The observed peaks corresponding to the reflection planes (211), (221), (301), (321), (141), and (061) provide clear evidence for the formation of a stibnite structure for the Sb_2Se_3 thin films under study. The detailed study of the as-deposited and selenized films registers the dominance of the preferred ($hk1$) peaks with the presence of two CdS compound peaks at $2\theta = 26.5$ and 52° (indicated with a star).[15,16] This is corroborated also by the XRD analysis of Sb_2Se_3 deposited on SnO_2, which does not show the abovementioned peaks (not shown). The predominance of the ($hk1$) orientations is a positive effect since it corresponds to the $(Sb_4Se_6)_n$ ribbons perpendicularly oriented on the substrate. This orientation improves drastically the carrier transport mechanism in the absorber. On the other hand, ($hk0$) peaks indicate that the grains are stacked horizontally on the substrate.[17]

The co-selenized samples show a reduced intensity of the CdS peaks, notably enhancing the presence of the (061) and (141) reflections. For the post-selenized samples, CdS detection is almost suppressed; moreover, an additional dominant (041) peak is observed. Note that no additional Se diffraction peaks are detected, despite the fact that Se supply is in excess during the in situ selenization process. As a matter of fact, the substrate temperature during Se evaporation is above the melting point of Se and thus excludes possible condensation of Se vapor into the sample.

The texture coefficient (TC) of a plane represents the texture of a particular plane whose deviation from the standard sample implies the preferred growth. It is calculated by the Harris formula (see eq 1):

$$T(hkl) = \frac{I_{(hkl)}}{I_{o(hkl)}} \left[\frac{1}{n} \sum_{i=1}^{N} \frac{I_{(hkl)}}{I_{o(hkl)}} \right]^{-1} \tag{1}$$

where $I_{(hkl)}$ is the measured diffraction peak intensity of the (hkl) plane, $I_{o(hkl)}$ is the standard XRD peak intensity, and n is the number of reflections considered for calculations.

A texture coefficient value larger than 1 indicates an enhanced texture orientation along that particular plane compared to the standard orientation.[18] The different texture coefficients highlight the difference in crystal orientation and quantitatively evaluate and compare the crystallite behavior when co-selenization and post-selenization are applied.

As shown in Figures 1−3, the Sb_2Se_3 layer grows spontaneously with a (221) high orientation; however, when the texture coefficient is calculated, we realize that (321) is also a very predominant peak, which is reduced in favor of the (141) orientation through post-deposition annealing or co-selenization. This last orientation is present together with the (041) peak when post-selenization is applied instead. In this

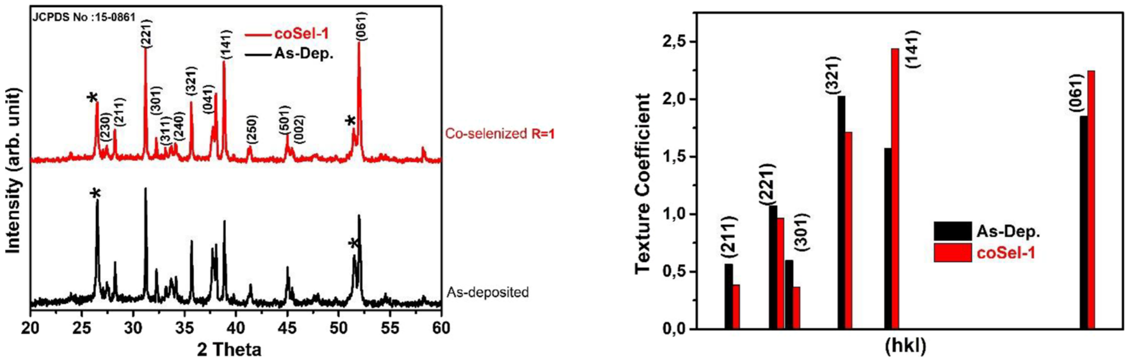

Figure 1. XRD spectra and TC of the as-deposited and co-selenized samples.

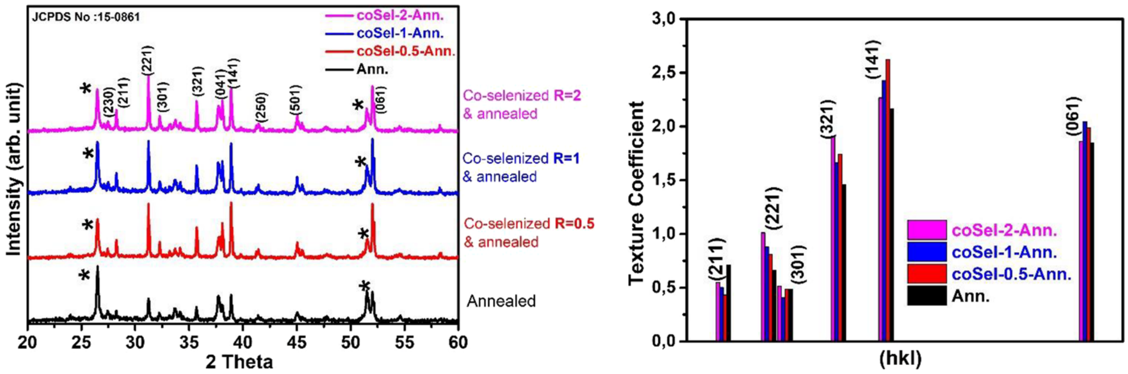

Figure 2. XRD spectra and TC of the vacuum-annealed sample and co-selenized samples.

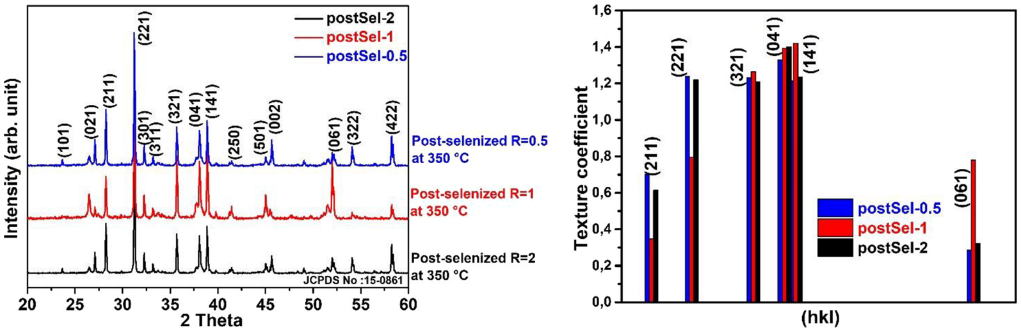

Figure 3. XRD spectra and TC of post-selenized samples.

case, the (221) orientation has a stronger incidence compared to the other cases, while the (061) peak is largely reduced.

This shows that despite the apparently similar spectra and the stronger (221) peak intensity, there is a different preferred orientation if the layer is subjected to post-deposition annealing, co-selenization, and post-deposition selenization. Also, this suggests that by adding selenium, we perform a different restructuring of the crystals, which moreover depends on the way of incorporating selenium.

We can observe that after annealing in vacuum (where we presume a slight Se loss), the main peaks have a reduced TC; this is also observed for co-selenized samples, while for post-deposition selenization, the original reflections are recovered, suggesting that the post-deposition selenization is able to keep the initial structure.

The crystallite size and lattice strain of the present samples are calculated by analyzing the peak broadening of the XRD pattern using Scherrer's formula (see eq 2):

$$d(hkl) = \frac{k\lambda}{ß \cos \theta} \tag{2}$$

where λ is the wavelength of X-ray radiation (1.5405 Å), θ is the Bragg's angle, ß is the FWHM (full width at half-maximum) in radians, and k is a constant related to the crystallite shape and is taken as 0.94.[19,20]

The microstrain (S) of the films is estimated by using the formula S = ß cos $\theta/4$. The average crystallite sizes and microstrain values for all the as-deposited, co-selenized, and post-selenized samples are presented in Table 2,ba, which clearly shows the increase in microstrain with the selenization rate for the post-selenization process. On the other hand, the average crystallite size of the thin films decreases from 71 to 53 nm with vacuum annealing; however, it is preserved near 70 nm with the co- and post-selenization processes.

By analyzing the spectra with Rietvield refinements[21] using the MAUD software,[22] we can observe that the lattice parameters of as-deposited, annealed, co-selenized, and post-

Table 2. Lattice Parameters and Average Crystallite Sizes of the (a) As-deposited and Co-selenized Sb_2Se_3 Thin Films and (b) Post-selenized Sb_2Se_3 Thin Films

(a) sample I.D.	lattice parameters (Å)	FWHM (221) and (141) (ß)	average crystallite (nm)	microstrain (*S*)
As-Dep.	a = 11.602, b = 11.764, c = 3.971	0.1215, 0.1270	71	4×10^{-3}
coSel-1		0.1245, 0.1175	71	6×10^{-3}
Ann.	a = 11.585, b = 11.764, c = 3.972	0.1465, 0.1520	53	6.9×10^{-3}
coSel-0.5-Ann.		0.1285, 0.1100	72	5.8×10^{-3}
coSel-1-Ann.	a = 11.593, b = 11.754, c = 3.970	0.1490, 0.1340	65	5.4×10^{-3}

(b) sample I.D.	lattice parameters (Å)	FWHM (221) and (141) (ß)	average crystallite (nm)	microstrain (*S*)
postSel-1	a = 11.616, b = 11.755, c = 3.970	0.1220, 0.1350	68	1.3×10^{-2}
postSel-0.5		0.1052, 0.0955	87	9.2×10^{-3}
postSel-2		0.1270, 0.1090	74	1×10^{-2}

selenized layers are different. In particular, the lattice parameters of the as-deposited absorber are in line with what has been measured and/or calculated from other laboratories.[11,23,19] Lattice parameters *b* and *c* are very similar irrespective of the different treatments; however, the lattice parameter *a* changes. In the as-deposited case, this value is 11.6 Å, quite similar to what is observed in the literature. However, it shrinks to 11.58 Å (negative displacement) when the absorber is annealed at 350 °C; this is also the case if the layer is deposited by co-selenization with a value of 11.59 Å. Otherwise, when the absorber is annealed at 350 °C in a selenium atmosphere, the *a*-value is repristinated to larger sizes, even closer to the standard value for Sb_2Se_3.[9] We have to observe that the microstrain for this last case is quite larger compared to the as-deposited case: probably, the positive displacement of the lattice parameter generates an evident microstrain. This is confirmed for each post-selenized case, demonstrating that the inclusion of selenium by post-selenization at 350 °C delivers a very different condition. As a matter of fact, the presence of selenium at high temperature recrystallizes the layer, possibly reducing the selenium vacancies and, for this reason, restoring the original *a*-lattice path. The result is a layer that stoichiometrically is not selenium-poor but at the same time has large grains (as observed in the crystallite size and in the following AFM images). The effectiveness of this treatment in mitigating the selenium deficiency is also suggested by the absence of the CdS peaks in the XRD spectra: probably, Se diffuses even in the window layer damaging it.

Figure 4 shows the top-view AFM images of the films, while Table 3 presents the root mean square (RMS) values, which indicate the roughness of the film, and the mean grain sizes of the samples. The AFM image of the as-deposited case exhibits dense, homogeneous, and relatively large grains (0.5−1 μm). After annealing in vacuum and/or co-selenization, the grains are smaller (less than 0.5 μm), with different more-round shapes and with a clear loss in compactness. No particular

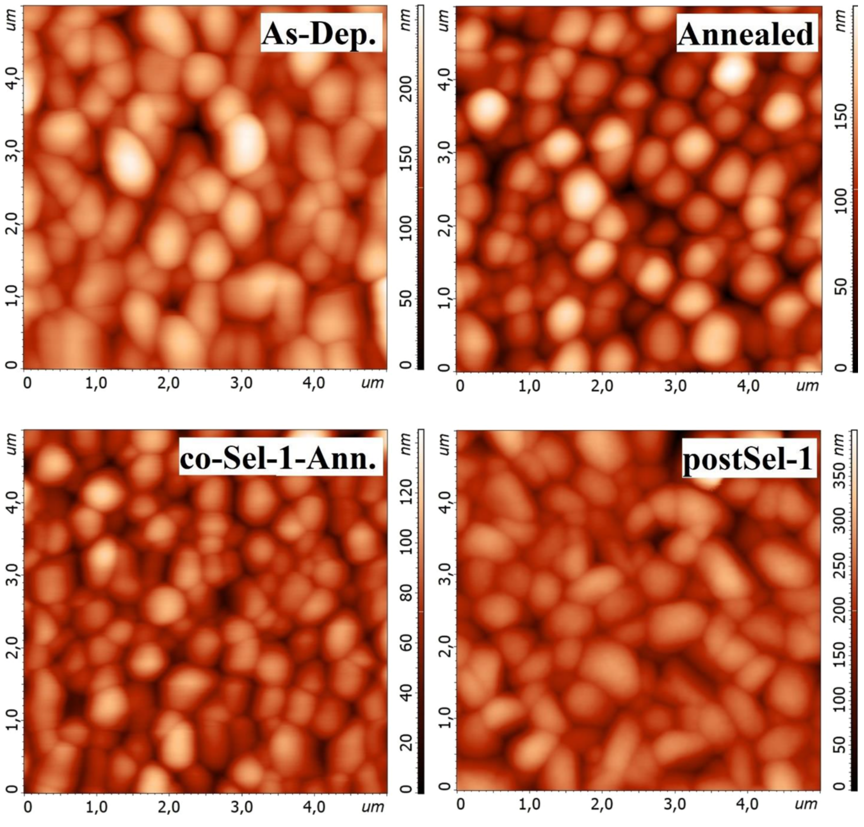

Figure 4. AFM images of the as-deposited, annealed, and co- and post-selenized samples.

Table 3. AFM Analysis (Refer to Figure 4) Showing the Root-Mean-Square (RMS) Roughness (Sq) Values and Mean Grain Sizes of the Samples

sample I.D.	RMS, Sq (nm)	mean grain size (nm)
As-Dep	31	511
Ann	32	479
coSel-1-Ann	20	368
postSel-1	43	554

difference in morphology is observed for the different Se evaporation rates.

On the other hand, when the layers are selenized after deposition, the surface presents a different morphology compared to the co-selenized ones. The grains are larger, reaching similar sizes of the as-deposited case, but with a much larger compactness: the boundaries are well overposed and the grains well aligned.

Again, we can observe, with co-selenization and/or post-deposition annealing, a change of the initial conditions, which results in reduction of grain size, which is coherent with the observed reduction of *a*-lattice parameters and crystallites.

In Figure 5, the SEM pictures of the as-deposited, annealed, co- and post-selenized samples confirm the morphology observed with AFM; however, these wider views give a clearer idea of the homogeneity of the structure: the enhanced grain size is even more evident for the post-selenized layer, while for the co-selenized and annealed absorbers, the reduction is confirmed.

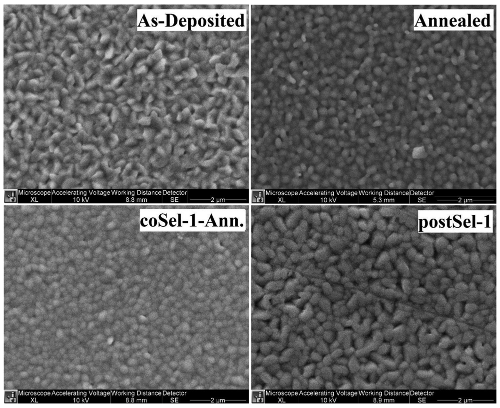

Figure 5. SEM pictures of the as-deposited, annealed, and co- and post-selenized samples.

The Raman spectra of the as-deposited, vacuum annealed, co-selenized, and post-selenized samples, shown in Figure 6, demonstrates the overall absence of large amounts of secondary phases. All the samples deliver a very similar spectrum, with the main Sb_2Se_3 peaks at the same position without evident shifts to highlight, indicating that during co-selenization as well as post-deposition selenization, no elemental selenium phase is formed and the stoichiometry is preserved.

In order to analyze the effect of Se inclusion on the cell performance, efficiencies together with the electrical parameters of the superstrate TEC/CdS/Sb_2Se_3/Au devices are summarized in Table 4,ba. Moreover, the *J*−*V* characteristics of the devices are presented in Figure 7.

Efficiencies are very different when as-deposited and annealed Sb_2Se_3 layers are compared, resulting actually in being, respectively, the lowest and the highest efficiencies of the set.

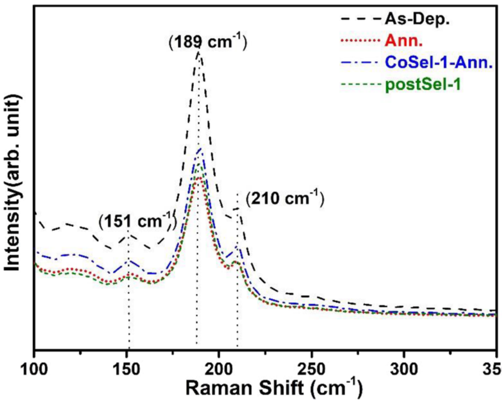

Figure 6. Raman spectra for the as-deposited, annealed, and co- and post-selenized Sb_2Se_3 thin films.

As a matter of fact, the best device with the as-deposited absorber layer shows an open circuit voltage (V_{oc}) of 289 mV, a fill factor (F.F.) of 45.4%, and a very low short circuit current density (J_{sc}) of 12 mA/cm^2, corresponding to a power conversion efficiency of 1.57%. Meanwhile, devices with absorber layers annealed in vacuum exhibit a V_{oc} of 352 mV, a J_{sc} of 23.5 mA/cm^2, and F.F. of 44%, resulting in an efficiency of 3.65%. All the parameters show a clear improvement, except for the fill factor, which remains equal; however, the 44−45% fill factor values are one of the highest obtained in the literature for low-temperature deposition.

For devices made with absorbers deposited by co-selenization at different rates (R = 2, R = 1, and R = 0.5), a maximum V_{oc} of 317 mV, J_{sc} of 25.8 mA/cm^2, and F.F. of 43.4% (conversion efficiency of 3.55%) are obtained in the R = 1 case. The champion cell of the post-selenized sample, again the R = 1 case, registers a PCE of 3.45%, V_{oc} of 345 mV, J_{sc} of 25 mA/cm^2, and F.F. of 40.7%. In any case, we can observe, for these kinds of devices, a further increase in current density.

This behavior can be explained if we examine the EQE presented in Figure 8. The device corresponding to the as-deposited absorber case shows a very low response on all ranges of wavelengths, which highlights a general low quality of the absorber material with a large loss in carrier collection. If the same absorber is annealed at 350 °C, the finished device shows a very good response, particularly near the junction (at the low wavelength region), while it loses response in the long wavelength region, where the photons are collected away from the junction near the back contact. On the other hand, the co-selenized absorber layers deliver devices that have a larger EQE response in the long wavelength region, in particular above 750 nm. However, these devices have a slight reduction in EQE in the 500 nm region, which suggests the deterioration of the junction. This explains why we measure a higher current density in these cases but the overall efficiency remains the same. If we now take into account the EQE of the devices made with post-deposition selenization, we register a further improvement of the EQE in the long wavelength region, and again the result is a slight increase in short current density. However, for these devices, the loss in the short wavelength region is even larger. This suggests that incorporation of additional selenium on the back improves the performance of the semiconductor by possibly increasing lifetime, reducing

Table 4. Statistics of Device Performance, Peak and Average, for Sb_2Se_3 Solar Cells with (a) As-deposited and Co-selenized Samples at Different Rates and (b) Post-selenized samples

(a) sample I.D.	V_{oc} (mV)	J_{sc} (mA/cm^2)	F.F. (%)	η (%)
As-Dep peak	289	12.0	45.4	1.57
As-Dep avg.	278 ± 4	11.8 ± 0.8	45.6 ± 0.2	1.5 ± 0.1
coSel-1 peak	345	22.2	39.7	3.05
coSel-1 avg.	347 ± 1	21.0 ± 0.4	40 ± 0.1	2.9 ± 0.1
Ann. peak	352	23.5	44.2	3.65
Ann. avg.	350 ± 2	22.3 ± 0.5	44.5 ± 0.2	3.5 ± 0.1
coSel-0.5-Ann. peak	324	25.3	42.6	3.50
coSel-0.5-Ann. avg.	326 ± 5	22.8 ± 0.7	43.4 ± 0.3	3.2 ± 0.1
coSel-1-Ann. peak	317	25.8	43.4	3.55
coSel-1-Ann. avg.	326 ± 3	24.0 ± 0.8	42.3 ± 0.4	3.3 ± 0.1
coSel-2-Ann. peak	324	22.9	39.0	2.89
coSel-2-Ann. avg.	320 ± 2	21.6 ± 0.5	40.1 ± 0.3	2.7 ± 0.1
(b) sample I.D.	V_{oc} (mV)	J_{sc} (mA/cm^2)	F.F. (%)	η (%)
postSel-0.5 peak	303	19.3	39.6	2.32
postSel-0.5 avg.	308 ± 2	18.1 ± 0.4	40.8 ± 0.3	2.3 ± 0.1
postSel-1 peak	345	25.0	40.0	3.45
postSel-1 avg.	346 ± 4	23 ± 1	39.4 ± 0.6	3.2 ± 0.1
postSel-2 peak	331	23.0	40.7	3.10
postSel-2 avg.	328 ± 2	22 ± 1	40.5 ± 0.2	2.9 ± 0.1

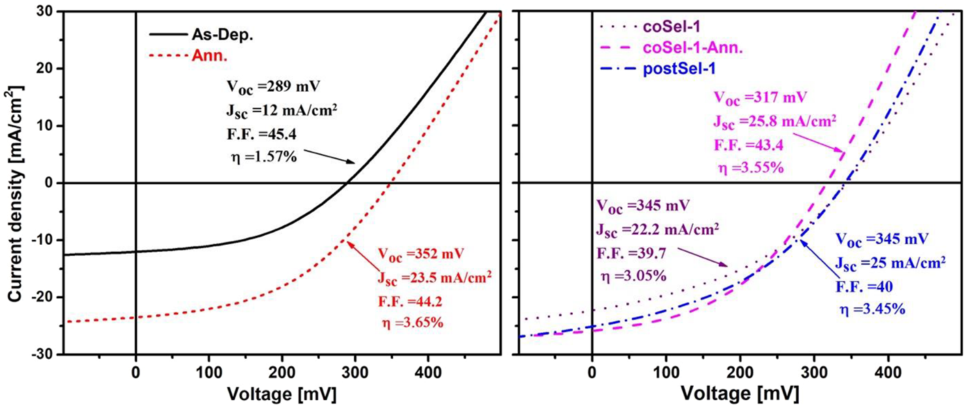

Figure 7. *J*−*V* curves of the as-deposited and annealed devices (left side) and of the co-selenized and post-selenized samples (right side).

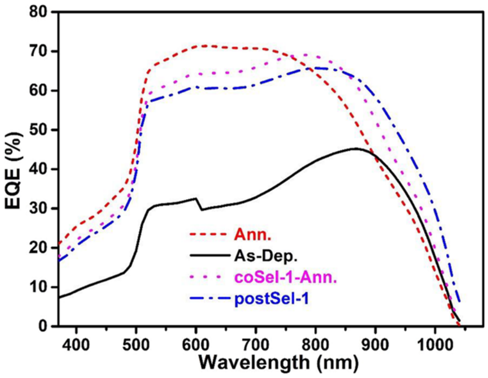

Figure 8. Corresponding EQE spectra of the as-deposited, annealed, and co- and post-selenized devices.

recombination effects, and enhancing the overall quality of the back contact.

The presence of CdS is clearly observed in the XRD for as-deposited and annealed absorbers, less observed in the co-selenized absorbers, and least observed in the post-deposition absorbers. The lower the CdS peaks, the lower the response in the short wavelength region, but at the same time, the higher the response at long wavelengths. The reduced detectability of CdS peaks, culminating in their almost total suppression in the post-selenized samples, suggests that there is a decomposition of the window layer at the junction due to the increased presence and diffusion of Se in the layer. In addition, in a previous study on $CdSe_xTe_{1-x}$-based solar cells,[24] we have already proven the degradation of CdS after the selenization of the layer above it. Moreover, the collapse of the EQE response occurs between 750 and 700 nm, which is the wavelength region corresponding to the band gap of CdSe (around 1.72 eV), indicating the possible formation of this not photoactive compound at the junction.[25] Thus, while the stoichiometry of the absorber is enhanced by co-selenization and even more by the post-selenization process, the quality of the junction deteriorates; the presence of CdS appears to be a limiting factor in improving the devices. A possible solution could be the replacement of CdS with a more suitable buffer layer, such as TiO_2.

In any case, we would like to highlight that the efficiencies reported between 3.5 and 3.65%, despite not being the highest in absolute terms, are to our knowledge the highest obtained with low-temperature vacuum evaporation and with a CdS buffer layer.

CONCLUSIONS

To summarize, we systematically investigated in situ selenization of the superstrate Sb_2Se_3 films. From the measurements and analysis, we conclude that selenization plays a key role in improving the absorber quality, possibly compensating Se loss, which occurs during thermal evaporation and vacuum annealing. The crystal growth is strongly affected by the co-selenization and/or post-deposition treatments, and Sb_2Se_3 layers show a good orientation at first by organizing along the *c* line perpendicular to the substrate. With co-selenization, the crystal structure changes, the CdS thickness is reduced, and the orientation of the grains is more randomly distributed; furthermore, the grain size is generally decreased and the *a*-lattice parameter is shrunk. However, the crystal quality improves when Se is added by post-deposition treatment, resulting in larger and more compact morphology. In this case, the *a*-lattice path is enlarged, getting closer to standard Sb_2Se_3 values, while the microstrain is observed. Finally, the presence of CdS peaks is almost totally suppressed.

The selenium treatments lead to an enhanced current density observed by $J-V$ characterization and confirmed by external quantum efficiency, where a remarkable gain at long wavelengths is observed; this effect is stronger for post-deposition selenium incorporation. However, the reduced response in the short wavelength range does not allow for champion efficiency. This is probably caused by the deterioration of the CdS layer due to the increased presence and diffusion of Se, which degrades the performance of the heterojunction. This process, with an optimized buffer layer, can be a base step for high-efficiency low-temperature growth Sb_2Se_3devices, with potential for flexible solar cells.

AUTHOR INFORMATION

Corresponding Author

Alessandro Romeo − *LAPS- Laboratory for Photovoltaics and Solid State Physics, Department of Computer Science, University of Verona, Verona 37134, Italy;* orcid.org/0000-0001-5068-8788; Phone: +39-045-8027974; Email: alessandro.romeo@univr.it

Authors

Vikash Kumar − *LAPS- Laboratory for Photovoltaics and Solid State Physics, Department of Computer Science, University of Verona, Verona 37134, Italy*

Elisa Artegiani − *LAPS- Laboratory for Photovoltaics and Solid State Physics, Department of Computer Science, University of Verona, Verona 37134, Italy*

Prabeesh Punathil − *LAPS- Laboratory for Photovoltaics and Solid State Physics, Department of Computer Science, University of Verona, Verona 37134, Italy*

Matteo Bertoncello − *Department of Information Engineering, University of Padova, Padova 35131, Italy*

Matteo Meneghini − *Department of Information Engineering, University of Padova, Padova 35131, Italy*

Fabio Piccinelli − *Solid State Chemistry Laboratory, Department of Biotechnology, University of Verona, Verona 37134, Italy;* orcid.org/0000-0003-3349-1960

Complete contact information is available at: https://pubs.acs.org/10.1021/acsaem.1c02301

Notes

The authors declare no competing financial interest.

ACKNOWLEDGMENTS

The Technological platform center at the University of Verona is thankfully acknowledged for Raman and XRD analysis.

REFERENCES

(1) Green, M. A.; Dunlop, E. D.; Hohl-Ebinger, J.; Yoshita, M.; Kopidakis, N.; Ho-Baillie, A. W. Y. Solar Cell Efficiency Tables (Version 55). *Progr. Photovolt.: Res. Appl.* **2020**, *28*, 3−15.

(2) Baranowski, L. L.; McLaughlin, K.; Zawadzki, P.; Lany, S.; Norman, A.; Hempel, H.; Eichberger, R.; Unold, T.; Toberer, E. S.; Zakutayev, A. Effects of Disorder on Carrier Transport in Cu_2SnS_3. *Phys. Rev. Appl.* **2015**, *4*, 1−9.

(3) Dittrich, H.; Bieniok, A.; Brendel, U.; Grodzicki, M.; Topa, D. Sulfosalts - A New Class of Compound Semiconductors for Photovoltaic Applications. *Thin Solid Films* **2007**, *515*, 5745−5750.

(4) Hartnauer, S.; Körbel, S.; Marques, M. A. L.; Botti, S.; Pistor, P.; Scheer, R. Research Update: Stable Single-Phase Zn-Rich $Cu_2ZnSnSe_4$ through in Doping. *APL Mater.* **2016**, *4*, 070701.

(5) Rampino, S.; Pattini, F.; Bronzoni, M.; Mazzer, M.; Sidoli, M.; Spaggiari, G.; Gilioli, E. $CuSbSe_2$ Thin Film Solar Cells with ∼4% Conversion Efficiency Grown by Low-Temperature Pulsed Electron Deposition. *Sol. Energy Mater. Sol. Cells* **2018**, *185*, 86−96.

(6) Tang, R.; Wang, X.; Lian, W.; Huang, J.; Wei, Q.; Huang, M.; Yin, Y.; Jiang, C.; Yang, S.; Xing, G.; Chen, S.; Zhu, C.; Hao, X.; Green, M. A.; Chen, T. Hydrothermal Deposition of Antimony Selenosulfide Thin Films Enables Solar Cells with 10% Efficiency. *Nat. Energy* **2020**, *5*, 587−595.

(7) Kumar, V.; Artegiani, E.; Kumar, A.; Mariotto, G.; Piccinelli, F.; Romeo, A. Effects of Post-Deposition Annealing and Copper Inclusion in Superstrate Sb2Se3 Based Solar Cells by Thermal Evaporation. *Sol. Energy* **2019**, *193*, 452−457.

(8) Pattini, F.; Rampino, S.; Mezzadri, F.; Calestani, D.; Spaggiari, G.; Sidoli, M.; Delmonte, D.; Sala, A.; Gilioli, E.; Mazzer, M. Role of the Substrates in the Ribbon Orientation of Sb_2Se_3 Films Grown by Low-Temperature Pulsed Electron Deposition. *Sol. Energy Mater. Sol. Cells* **2020**, *218*, 110724.

(9) Zhou, Y.; Leng, M.; Xia, Z.; Zhong, J.; Song, H.; Liu, X.; Yang, B.; Zhang, J.; Chen, J.; Zhou, K.; Han, J.; Cheng, Y.; Tang, J. Solution-Processed Antimony Selenide Heterojunction Solar Cells. *Adv. Energy Mater.* **2014**, *4*, 1301846.

(10) Zeng, K.; Xue, D. J.; Tang, J. Antimony Selenide Thin-Film Solar Cells. *Semicond. Sci. Technol.* **2016**, *31*, No. 063001.

(11) Mavlonov, A.; Razykov, T.; Raziq, F.; Gan, J.; Chantana, J.; Kawano, Y.; Nishimura, T.; Wei, H.; Zakutayev, A.; Minemoto, T.; Zu, X.; Li, S.; Qiao, L. A Review of Sb2Se3 Photovoltaic Absorber Materials and Thin-Film Solar Cells. *Sol. Energy* **2020**, *201*, 227−246.

(12) Li, Z.; Liang, X.; Li, G.; Liu, H.; Zhang, H.; Guo, J.; Chen, J.; Shen, K.; San, X.; Yu, W.; Schropp, R. E. I.; Mai, Y. 9.2%-Efficient Core-Shell Structured Antimony Selenide Nanorod Array Solar Cells. *Nat. Commun.* **2019**, *10*, 125.

(13) Luo, M.; Leng, M.; Liu, X.; Chen, J.; Chen, C.; Qin, S.; Tang, J. Thermal Evaporation and Characterization of Superstrate CdS/Sb 2Se3 Solar Cells. *Appl. Phys. Lett.* **2014**, *104*, 173904.

(14) Liu, X.; Chen, J.; Luo, M.; Leng, M.; Xia, Z.; Zhou, Y.; Qin, S.; Xue, D. J.; Lv, L.; Huang, H.; Niu, D.; Tang, J. Thermal Evaporation and Characterization of Sb2Se3thin Film for Substrate Sb2Se3/CdS Solar Cells. *ACS Appl. Mater. Interfaces* **2014**, *6*, 10687−10695.

(15) Maiti, A.; Chatterjee, S.; Pal, A. J. Sulfur-Vacancy Passivation in Solution-Processed Sb_2S_3 Thin Films: Influence on Photovoltaic Interfaces. *ACS Appl. Energy Mater.* **2020**, *3*, 810−821.

(16) Zhou, Y.; Li, Y.; Luo, J.; Li, D.; Liu, X.; Chen, C.; Song, H.; Ma, J.; Xue, D. J.; Yang, B.; Tang, J. Buried Homojunction in CdS/Sb_2Se_3 Thin Film Photovoltaics Generated by Interfacial Diffusion. *Appl. Phys. Lett.* **2017**, *111*, 013901.

(17) Li, D. B.; Yin, X.; Grice, C. R.; Guan, L.; Song, Z.; Wang, C.; Chen, C.; Li, K.; Cimaroli, A. J.; Awni, R. A.; Zhao, D.; Song, H.; Tang, W.; Yan, Y.; Tang, J. Stable and Efficient CdS/Sb_2Se_3 Solar Cells Prepared by Scalable Close Space Sublimation. *Nano Energy* **2018**, *49*, 346−353.

(18) Guo, L.; Grice, C.; Zhang, B.; Xing, S.; Li, L.; Qian, X.; Yan, F. Improved Stability and Efficiency of CdSe/Sb_2Se_3 Thin-Film Solar Cells. *Sol. Energy* **2019**, *188*, 586−592.

(19) Polivtseva, S.; Adegite, J. O.; Kois, J.; Mamedov, D.; Karazhanov, S. Z.; Maricheva, J.; Volobujeva, O. A Novel Thermochemical Metal Halide Treatment for High-Performance Sb2Se3 Photocathodes. *Nanomaterials* **2021**, *11*, 1−14.

(20) Mathew, N. J.; Oommen, R. STRUCTURAL AND MORPHOLOGICAL STUDIES OF Sb 2 S 3 THIN FILMS. *J. Ovonic Res.* **2010**, *6*, 259−266.

(21) Paufler, P. R. A.Young (Ed.). The Rietveld Method. International Union of Crystallography. Oxford University Press 1993. 298 p. Price £ 45.00. ISBN 0−19−855577−6. *Cryst. Res. Technol.* **1995**, *30*, 494.

(22) Lutterotti, L.; Gialanella, S. X-Ray Diffraction Characterization of Heavily Deformed Metallic Specimens. *Acta Mater.* **1998**, *46*, 101.

(23) Deringer, V. L.; Stoffel, R. P.; Wuttig, M.; Dronskowski, R. Vibrational Properties and Bonding Nature of Sb_2Se_3 and Their Implications for Chalcogenide Materials. *Chem. Sci.* **2015**, *6*, 5255−5262.

(24) Artegiani, E.; Gasparotto, A.; Punathil, P.; Kumar, V.; Barbato, M.; Meneghini, M.; Meneghesso, G.; Piccinelli, F.; Romeo, A. A New Method for CdSexTe1-x Band Grading for High Efficiency Thin-Absorber CdTe Solar Cells. *Sol. Energy Mater. Sol. Cells* **2021**, *226*, 111081.

(25) Spalatu, N.; Krautmann, R.; Katerski, A.; Karber, E.; Josepson, R.; Hiie, J.; Acik, I. O.; Krunks, M. Screening and Optimization of Processing Temperature for Sb2Se3 Thin Film Growth Protocol: Interrelation between Grain Structure, Interface Intermixing and Solar Cell Performance. *Sol. Energy Mater. Sol. Cells* **2021**, *225*, 111045.